

---

**1 Revisiting the Austral Spring Extratropical Southern  
2 Hemisphere zonally assymetric circulation using  
3 complex Empirical Orthogonal Functions**

**4 Elio Campitelli · Leandro B. Díaz ·  
5 Carolina Vera ·**

**6**  
**7 Received: date / Accepted: date**

**8 Abstract** abstract

**9**

**10 Keywords** ·

---

The research was supported by UBACyT20020170100428BA and the CLIMAX Project funded by Belmont Forum/ANR-15-JCL/-0002-01. Elio Campitelli was supported by a PhD grant from CONICET, Argentina.

Elio Campitelli  
Universidad de Buenos Aires, Facultad de Ciencias Exactas y Naturales, Departamento de Ciencias de la Atmósfera y los Océanos. Buenos Aires, Argentina.  
CONICET – Universidad de Buenos Aires. Centro de Investigaciones del Mar y la Atmósfera (CIMA). Buenos Aires, Argentina.  
CNRS – IRD – CONICET – UBA. Instituto Franco-Argentino para el Estudio del Clima y sus Impactos (IRL 3351 IFAECI). Buenos Aires, Argentina.  
E-mail: [elio.campitelli@cima.fcen.uba.ar](mailto:elio.campitelli@cima.fcen.uba.ar)

Leandro B. Díaz  
Universidad de Buenos Aires, Facultad de Ciencias Exactas y Naturales, Departamento de Ciencias de la Atmósfera y los Océanos. Buenos Aires, Argentina. CONICET – Universidad de Buenos Aires. Centro de Investigaciones del Mar y la Atmósfera (CIMA). Buenos Aires, Argentina. CNRS – IRD – CONICET – UBA. Instituto Franco-Argentino para el Estudio del Clima y sus Impactos (IRL 3351 IFAECI). Buenos Aires, Argentina.

Carolina Vera  
Universidad de Buenos Aires, Facultad de Ciencias Exactas y Naturales, Departamento de Ciencias de la Atmósfera y los Océanos. Buenos Aires, Argentina. CONICET – Universidad de Buenos Aires. Centro de Investigaciones del Mar y la Atmósfera (CIMA). Buenos Aires, Argentina. CNRS – IRD – CONICET – UBA. Instituto Franco-Argentino para el Estudio del Clima y sus Impactos (IRL 3351 IFAECI). Buenos Aires, Argentina.

---

## 11 1 Introduction

### introduction

12 The large-scale extratropical circulation in the Southern Hemisphere is strongly  
 13 zonally symmetric, but its zonal departures are highly relevant for surface im-  
 14 pacts and could be related to high-impact climate extremes. Zonal asymme-  
 15 tries of extratropical circulation in the Southern Hemisphere strongly modulate  
 16 weather systems and regional climate through latitudinal transport of heat,  
 17 humidity, and momentum (Trenberth, 1980).

18 One of the main features of the zonally asymmetric circulation are the  
 19 Pacific–South American Patterns (Mo and Paegle, 2001), which are associ-  
 20 ated with precipitation anomalies in South America. Besides, Raphael (2007)  
 21 suggests that variability in the planetary wave 3 projected onto its climato-  
 22 logical location is associated with Antarctic sea ice concentration anomalies.  
 23 Irving and Simmonds (2015) showed that planetary wave amplitude in general  
 24 is associated sea ice concentration, as well as temperature and precipitation  
 25 anomalies.

26 Some of these patterns of variability associated to the zonally asymmet-  
 27 ric circulation appear to have experienced secular changes, although to our  
 28 knowledge this has not been extensively studied. For instance, Raphael (2003)  
 29 found that the amplitude of the zonal wave 1 experienced a large increase and  
 30 that the zonal wave 3 experienced changes in its annual cycle between 1958  
 31 and 1996.

32 One typical way of describing the zonally asymmetric circulation is by  
 33 the amplitude and phase of zonal waves obtained by Fourier decomposition  
 34 of geopotential height at each latitude (e.g. van Loon and Jenne, 1972; Tren-  
 35 berth, 1980; Turner et al, 2017). This approach suggests that zonal waves 1 and  
 36 3 explained most of the variance of the tropospheric extratropical Southern  
 37 Hemisphere circulation (van Loon and Jenne (1972)). However, this method-  
 38 ology relies on the assumption that the circulation can be meaningfully un-  
 39 derstood in terms of zonal waves of constant amplitude along a latitude circle.  
 40 This is not valid for meridionally propagating waves or zonal waves with lo-  
 41 calised amplitudes. In the case of the wave 3, for example, Trenberth and Mo  
 42 (1985) observed that it played a role in blocking events, but this was mostly  
 43 due to increased amplitude of a longitudinally localised wave train instead of  
 44 an hemispheric-scale zonal wave 3.

45 The fourier technique can be generalised to integrate all planetary wave in-  
 46 tensity irregardless of wave number by computing the wave envelope as done  
 47 by Irving and Simmonds (2015). This makes it possible to represent plane-  
 48 tary waves with different amplitude at different longitudes, but it removes all  
 49 information about phase and wave number.

50 Another approach to characterising the Southern Hemisphere circulation is  
 51 by using Empirical Orthogonal Functions (EOF, also known as Principal Com-  
 52 ponent Analysis). Within the EOF framework, the Southern Annular Mode  
 53 (SAM) appears as the leading mode of variability of the tropospheric South-  
 54 ern Hemisphere circulation (Fogt and Marshall, 2020) followed by the two  
 55 PSA (Mo and Paegle, 2001). The SAM represents a relatively zonally sym-

metric pattern of alternating low pressures in polar latitude and a ring of high pressures in high latitudes with an embedded wave 3 pattern that is more prominent in the Pacific sector. The PSA1 and PSA2 describe the two out-of-phase sides of a meridionally propagating wave train that originates in the Eastern equatorial Pacific and travels towards the South Atlantic following a great-circle arch along the Antarctic Peninsula. These patterns are derived by applying EOF to temporal anomalies, but Raphael (2003) applied EOF methods specifically to zonal anomalies.

EOFs are more flexible than Fourier decomposition modes in the sense that they can capture oscillation patterns that cannot be characterised by purely sinusoidal waves with constant amplitude. Nonetheless, they are restricted to standing oscillation modes and could not represent properly propagating or phase-varying modes such as zonal waves. A single EOF can also represent a mixture of two or more physical modes. The inability of a single EOF to describe travelling waves is what forces the PSA pattern to be described by two EOFs. Irving and Simmonds (2016) characterises this pattern in a Fourier framework. Being a meridionally propagating mode, the PSA cannot be correctly characterised by Fourier decomposition at each latitude circle. As a result, they reprojected meridional wind fields so that the path of the PSA laid on the equator. On this new projection, they could identify the PSA using Fourier decomposition.

Finally, another, hybrid, methodology commonly used consist on identifying particular features of interest and creating indices using simple methods such as averages and differences. The Marshal SAM Index (Marshall, 2003), for example, tries to characterise the SAM by the average difference of sea level pressure between 40°S and 65°S, following Gong and Wang (1999). Raphael (2004) used a similar methodology to describe the wave 3 in the Southern Hemisphere. Instead of using Fourier to compute the amplitude and phase of the zonal wave, they averaged standardised geopotential height anomalies in three points representing the location of the ridges of the zonal wave 3 of the climatological mean. This is equivalent to an index of the amplitude of the zonal wave 3 that projects into the phase of the zonal wave 3 of the mean field. Similarly, Hobbs and Raphael (2010) propose that the zonally asymmetric circulation in the Southern Hemisphere can be described by the strength and location of two anticyclones located in the sub-Antarctic western hemisphere. These methods are grounded on other methods to identify the centres of action for the described phenomena and can be useful to characterise features that are not readily apparent with Fourier or EOF methods. The use of data of only specific regions or locations makes them suitable for easy computation and for extending back into the data-poor past, but also makes them not very robust and unable to capture non-stationary patterns.

Our objective is to improve our understanding of planetary waves in the Southern Hemisphere using an index that is able to capture the phase-varying nature of planetary waves and is flexible enough to describe planetary waves with non-constant amplitude in each latitude circle. We use complex Empirical Orthogonal Functions (Horel, 1984) as a robust extension of EOF analysis that

102 is capable of describing rich structures with meridional and zonal propagation,  
 103 and amplitude modulation such as the PSA.

104 We apply this method to characterise the Springtime zonally asymmetric  
 105 circulation of the extratropical Southern Hemisphere. To take vertical distri-  
 106 bution into account, we analyse both the troposphere and the stratosphere.  
 107 We focus the analysis to the September-October-November because that's the  
 108 trimester in which tropical forcing of zonal waves is maximised (cita). **Este**  
 109 **parráfo me parece que quedo un poco colgado. Creo que sería importante que**  
 110 **esté desde más arriba la idea de la primavera, ya que todo lo otro es muy**  
 111 **general, pero al final el análisis solo se va a restringir a esta estación**

112 In Section 2 we describe the methods. In Section 3.1, we analyse the spatial  
 113 patterns of each complex EOF. In Section 3.2 we study the spatial regressions  
 114 with geopotential height and temperature. In Section 3.3, we analyse the rel-  
 115ationship between cEOF1 and Ozone, and between EOF2 and the Southern  
 116 Annular Mode and the PSA. In Section 3.4 we look for tropical forcings that  
 117 explain the variability of each cEOF. Finally, in Section 3.5 we show the rela-  
 118tionship between these modes of variability and precipitation in South America  
 119 and Oceania.

## 120 2 Data and Methods

121 **2.1 Data**

122 We used monthly geopotential height, air temperature, ozone mixing ratio,  
 123 and total ozone column (TOC) at  $2.5^\circ$  longitude by  $2.5^\circ$  latitude of hori-  
 124zontal resolution and 37 vertical isobaric levels from the European Centre  
 125 for Medium-Range Weather Forecasts Reanalysis version 5 [ERA; Hersbach  
 126 et al (2019)] for the period 1979-2019. Most of our analysis was restricted to  
 127 the post-satellite era to avoid any confounding factors arising from the in-  
 128corporation of satellite observations, but we also used the preliminary back  
 129 extension of ERA5 from 1950 to 1978 (Bell et al, 2020) to look at long-term  
 130 trends. Streamfunction was derived from ERA5 vorticity at 200 hPa using the  
 131 FORTRAN subroutine FISHPACK (Adams et al, 1999) and horizontal wave  
 132 activity fluxes was computed following Plumb (1985). We used Sea Surface  
 133 Temperature (SST) monthly fields from Extended Reconstructed Sea Surface  
 134 Temperature (ERSST) v5 (Huang et al, 2017) and precipitation monthly data  
 135 from the CPC Merged Analysis of Precipitation (Xie and Arkin, 1997), with a  
 136  $2.5^\circ$  resolution in latitude and longitude. This rainfall gridded dataset is based  
 137 on information from different sources such as rain gauge observations, satellite  
 138 inferred estimations and the NCEP-NCAR reanalysis, and it is available since  
 139 1979 to present.

---

140 2.2 Methods

methods-1

141 The study is restricted to the spring season, defined as the September-October-  
142 November (SON) trimester. We compute seasonal means for the different vari-  
143 ables, averaging monthly values weighted by the number of days in each month.  
144 We use 200 hPa level to represent the high troposphere and 50 hPa to represent  
145 the lower stratosphere.

146 The amplitude of the zonal waves was obtained through the Fourier trans-  
147 form of the spatial field at each latitude circle. We computed the amplitude  
148 and phase of the zonal wave 1 by averaging (area-weighted) each variable be-  
149 tween 75°S and 45°S for each SON and extracting the wave-1 component of  
150 the Fourier spectrum. We chose this latitude band because it is wide enough to  
151 capture most of the relevant anomalies for southern hemisphere mid-latitudes.

152 We computed the level-dependent SAM index as the leading EOF of year-  
153 round monthly geopotential height anomalies south of 20°S at each level for the  
154 whole period according to Baldwin and Thompson (2009). We further split the  
155 SAM into its zonally symmetric and zonally asymmetric components (S-SAM  
156 and A-SAM indices respectively). These indices were obtained by projecting  
157 the zonally asymmetric and zonally symmetric part of the SAM spatial pattern  
158 onto monthly geopotential height fields, as proposed by Campitelli et al (2021).  
159 Seasonal indices of the Pacific South American patterns (PSA1 and PSA2)  
160 were calculated following Mo and Paegle (2001) as the third and fourth leading  
161 EOF of seasonal mean anomalies for SH 500 hPa geopotential height combining  
162 all seasons. In our study, only the SON values were used.

163 Linear trends were computed by Ordinary Least Squares (OLS) and the  
164 95% confidence interval was computed assuming a t-distribution with the ap-  
165 propriate residual degrees of freedom (Wilks, 2011).

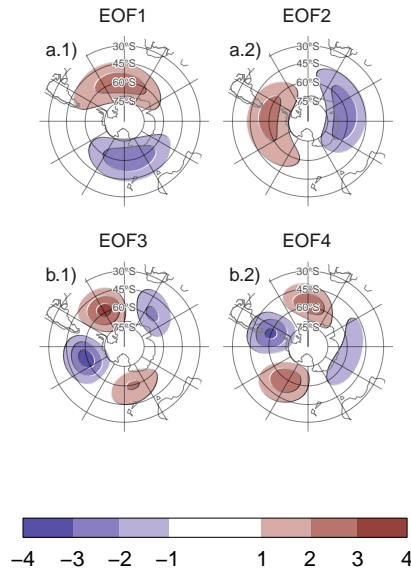
166 2.3 Complex Empirical Orthogonal Functions (cEOF)

complex-empirical-orthogonal-functions-ceof

167 **En la figura 1 te quedaron muy chicos los subplots, amplialos un poco.**

168 In traditional EOF analysis zonal waves appear as pairs of EOFs, that  
169 could be degenerated representing similar patterns but shifted in phase (Horel,  
170 1984). For instance, Figure 1 shows the leading 4 EOFs of SON geopotential  
171 height zonal anomalies at 50 hPa south of 20°S. It is clear that the first two  
172 EOFs represent the same zonal wave 1 pattern and the last two represent a  
173 same zonal wave pattern with shorter wavenumber and four centers of action  
174 shifted by 1/4 wavelength. A similar EOF structure can be seen in 200 hPa  
175 (not shown). Since each pair of EOFs seem to represent the same phase-varying  
176 structure, it would be desirable to combine them into a single index with  
177 amplitude and phase.

178 Complex Empirical Orthogonal Functions (cEOF) is a useful method to  
179 characterise zonal waves, considering phase-varying structures (Horel, 1984).  
180 This method involves computing EOF on the analytic representation of the  
181 original field. This representation is a complex field in which the real part is the



`fig:eof-naive`  
Fig. 1: Spatial patterns of the leading 4 EOFs of SON zonal anomalies of geopotential height at 50 hPa south of 20°S for the 1979 – 2019 period (arbitrary units).

182 original variable and the imaginary part is the original data shifted by 90° at  
 183 each spectral frequency – i.e. its Hilbert transform. The Hilbert transform is  
 184 usually understood in terms of time-varying signal. However, in this work we  
 185 apply the Hilbert transform to each latitude circle at each moment in time.  
 186 Since each latitude circle is a periodic domain, this procedure does not suffer  
 187 from edge effects.

188 The result of the cEOF methodology is a set of complex spatial patterns  
 189 and complex time series. The real and imaginary part of each spatial pattern  
 190 represent two phases wave-like spatial patterns that are in quadrature. The  
 191 magnitude and argument of each complex time series represent the amplitude  
 192 and phase of each zonal wave.

193 *Los colores de la Tabla 1 no dicen mucho en la medida que no se conoce  
 194 cuál sería la paleta. Quizás se pueden remarcar en negrita ambos aclarando  
 195 que son significativos (lo son?).*

196 The cEOF methodology is applied to SON geopotential height zonal anomalies  
 197 south of 20°S at 50 and 200 hPa, representing a stratospheric and upper  
 198 tropospheric level respectively. Table 1 shows the coefficient of determination  
 199 between time series of the amplitude of each complex EOF (cEOF) across  
 200 levels. There's a high degree of correlation between the magnitude of the re-  
 201 spective cEOF1 and cEOF2 at each level. The spatial patterns of the 50 hPa  
 202 and 200 hPa cEOFs are also similar (not shown).

203 Both the spatial pattern similarity and the high temporal correlation of  
 204 cEOFs computed at 50 hPa and 200 hPa suggest that these are, to a large

tab:corr-ceof-splitted  
Table 1: Coefficient of determination ( $R^2$ ) of the absolute magnitude of complex EOFs between 200 hPa and 50 hPa computing EOF separately for each level. Background colour indicates the value of  $R^2$ .

		50 hPa		
200 hPa		cEOF1	cEOF2	cEOF3
cEOF1	0.28	0.01	0.02	
cEOF2	0.00	0.60	0.02	
cEOF3	0.00	0.00	0.02	

205 extent, modes of joint variability. This motivates the decision of performing  
 206 complex EOF jointly between levels. The computation of the cEOFs was car-  
 207 ried out using data from both levels at the same time, therefore, each cEOF  
 208 has a spatial component that depends on longitude, latitude and level, and a  
 209 temporal component that depends only on time.

210 The phase of principal components is defined up to an additive constant.  
 211 For real principal components, this constant can be either 0 or  $\pi$ , correspond-  
 212 ing to a change in sign. For complex principal components, it can be any  
 213 number between 0 and  $2\pi$  (Horel, 1984). Since any choice is arbitrary and  
 214 equally valid, we chose the phase of each cEOF so that the real and imaginary  
 215 parts are aligned with meaningful phases in our analysis. This procedure does  
 216 not create a spurious correlation, it only takes a known relationship and aligns  
 217 it with a specific phase. For the first complex principal component, the phase  
 218 was chosen so that the time series corresponding to the real part has the max-  
 219 imum correlation with the zonal wave 1 of Total Ozone Column between 75°S  
 220 and 45°S. This also nearly minimises the correlation with the imaginary part.  
 221 For the second complex principal component, the phase was chosen so that  
 222 the coefficient of determination between the Oceanic Niño Index (Bamston  
 223 et al, 1997) and the real part was minimized, which also nearly maximizes the  
 224 correlation with the imaginary part.

225 While we compute these complex principal components using data from  
 226 1979 to 2019, we extended the complex time series back to the 1950 – 1978  
 227 period by projecting monthly geopotential height zonal anomalies standardised  
 228 by level south of 20°S onto the corresponding spatial patterns.

229 We performed linear regressions to quantify the association between the  
 230 cEOFs and other variables. For each cEOF, we create regression maps by  
 231 fitting a multiple linear model involving both the real and the imaginary part.  
 232 To obtain the linear coefficients of a variable  $X$  (geopotential, temperature,  
 233 precipitation, etc...) with the Imaginary and Real parts of each cEOF we fit  
 234 the equation

$$X(\lambda, \phi, t) = \alpha(\lambda, \phi) \operatorname{Im}(\text{cEOF}) + \beta(\lambda, \phi) \operatorname{Re}(\text{cEOF}) + X_0(\lambda, \phi) + \epsilon(\lambda, \phi, t)$$

235 where  $\lambda$  and  $\phi$  are the longitude and latitude,  $t$  is the time,  $\alpha$  and  $\beta$  are  
 236 the linear regression coefficients for Imaginary and Real parts respectively,  $X_0$   
 237 and  $\epsilon$  are the constant and error terms respectively.

238 We evaluated statistical significance using a two-sided t-test and, in the  
 239 case of regression maps, p-values were adjusted by controlling for the False  
 240 Discovery Rate (Benjamini and Hochberg, 1995; Wilks, 2016) to avoid mis-  
 241 leading results from the high number of regressions (Walker, 1914; Katz and  
 242 Brown, 1991).

## 243 2.4 Computation procedures

244 We performed all analysis in this paper using the R programming language  
 245 (R Core Team, 2020), using data.table (Dowle and Srinivasan, 2020) and  
 246 metR (Campitelli, 2020) packages. All graphics are made using ggplot2 (Wick-  
 247 ham, 2009). We downloaded data from reanalysis using the ecmwfr package  
 248 (Hufkens, 2020) and indices of the ENSO with the rsoi package (Albers and  
 249 Campitelli, 2020). The paper was rendered using knitr and rmarkdown (Xie,  
 250 2015; Allaire et al, 2020).

## 251 3 Results

### 252 3.1 cEOF spatial patterns

253 To describe the variability of the circulation zonal anomalies, the spatial and  
 254 temporal parts of the first two leading cEOFs of zonal anomalies of geopotential  
 255 height at 50 hPa and 200 hPa, computed jointly at both levels, are shown in  
 256 Figures 2 and 3. The first mode (cEOF1) explains 82% of the variance, while  
 257 the second mode (cEOF2) explains a smaller fraction (7%). In the spatial  
 258 patterns (Fig. 2), the real and the imaginary components are in quadrature  
 259 by construction, so that each cEOF describe a single wave-like pattern whose  
 260 amplitude and position (i.e. phase) is controlled by the magnitude and phase  
 261 of the temporal cEOF. The wave patterns described by these cEOFs match  
 262 the patterns seen in the traditional EOFs of Figure 1.

263 tengo la impresión de que en la figura 2 podría estar un poco más grandes  
 264 los subplots para se vean más fácilmente los detalles

265 The cEOF1 (Fig. 2 column a) is a hemispheric wave 1 pattern with maxi-  
 266 mum amplitude at high latitudes. At 50 hPa the Real cEOF1 has the maximum  
 267 of the wave 1 at 150°E and at 200 hPa, the maximum is located at around  
 268 175°E indicating a westerly shift in phase. The cEOF2 (Fig. 1 column b) shows  
 269 also a zonal wave-like structure with maximum amplitude at high latitudes,  
 270 but with shorter spatial scales. In particular, its dominant structure at both  
 271 levels is a wave 3 but with larger amplitude in the pacific sector. This modu-  
 272 lated amplitude is especially apparent at 200 hPa. There is no apparent phase  
 273 shift but the amplitude of the pattern is greatly reduced in the stratosphere,

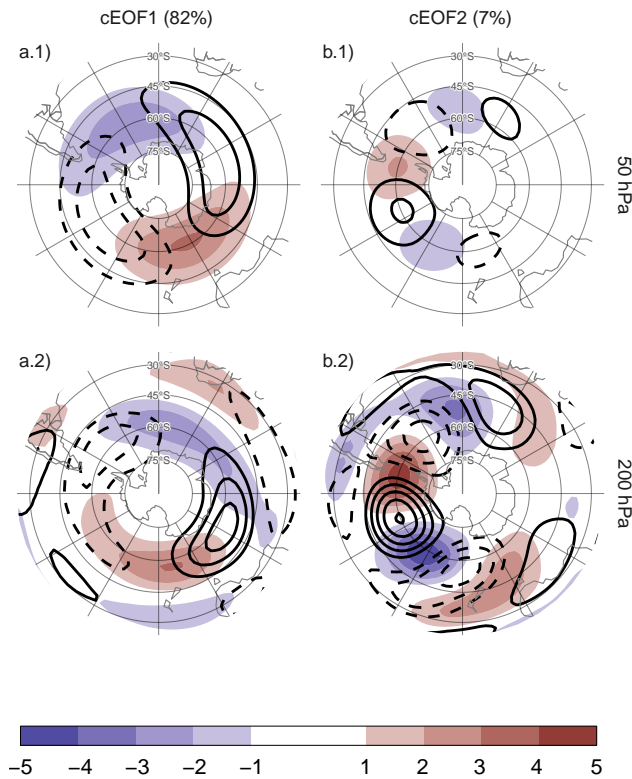


fig:ceofs-1  
Fig. 2: Spatial patterns for the two leading cEOFs of SON zonal anomalies of geopotential height at 50 hPa and 200 hPa for the 1979 – 2019 period. The shading (contours) corresponds to real (imaginary) part. Arbitrary units.

274 suggesting that this barotropic mode represents mainly tropospheric variability.  
275

276 se me vino una duda, ¿se pueden comparar de algún modo las amplitudes  
277 que mostras en esta figura? en caso de que si, creo que habría que mencionar  
278 algo sobre lo que pasa con el cEOF2 en la estratosfera All cEOFs have non  
279 zero mean (Fig. 3) because the geopotential fields that enter into the cE-  
280 OFs algorithm are anomalies with respect to the zonal mean instead of the  
281 time mean. However, cEOF2's mean is almost zero, which indicates that only  
282 cEOF1 includes variability that significantly projects onto the mean zonally  
283 anomalous field. There are no significant simultaneous correlation between the  
284 time series. Both cEOFs show year-to-year variability but show no evidence of  
285 decadal variability.

286 En la figura 3 agregaría dos cosas: i)el eje y en la columna derecha (si la  
287 queres ver más grande perdes la referencia) ii) creo que serviría agregar una  
288 líneas verticales en la grilla para poder tener una idea un poco mejor de a  
289 qué años corresponde más o menos cada valor. pueden ser un poco más finas

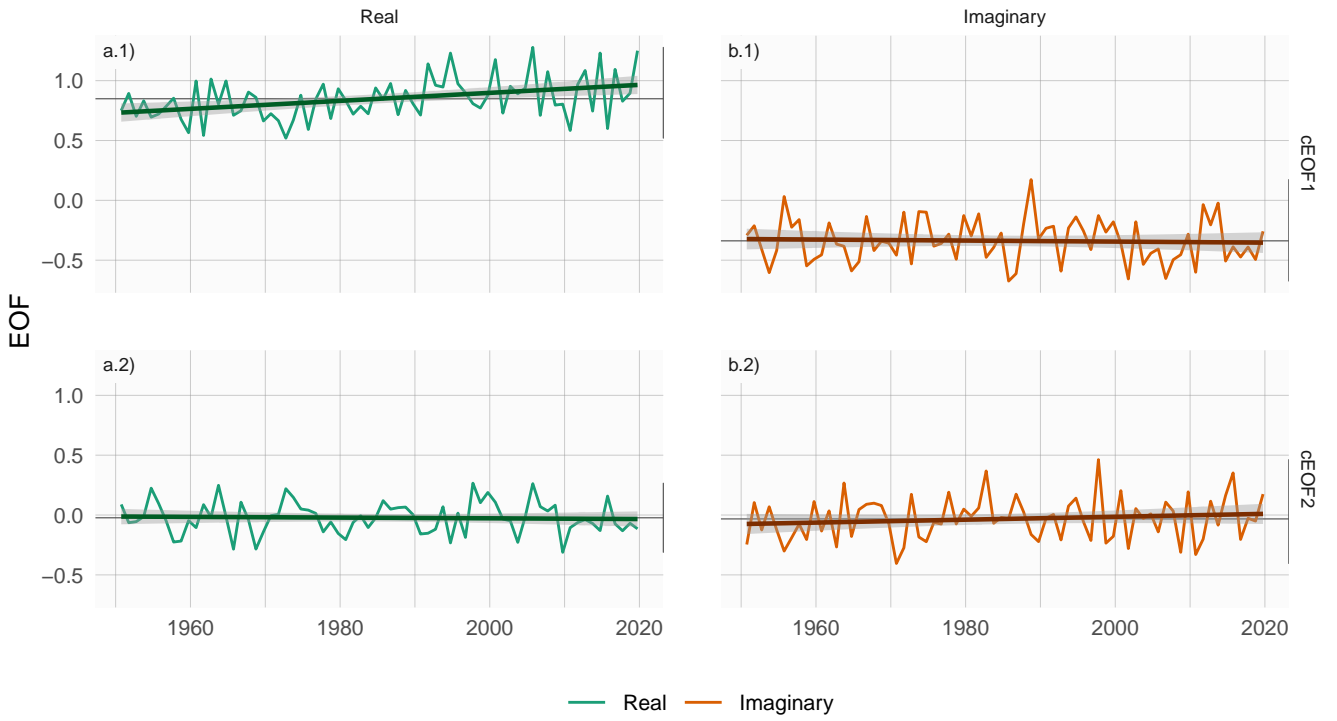
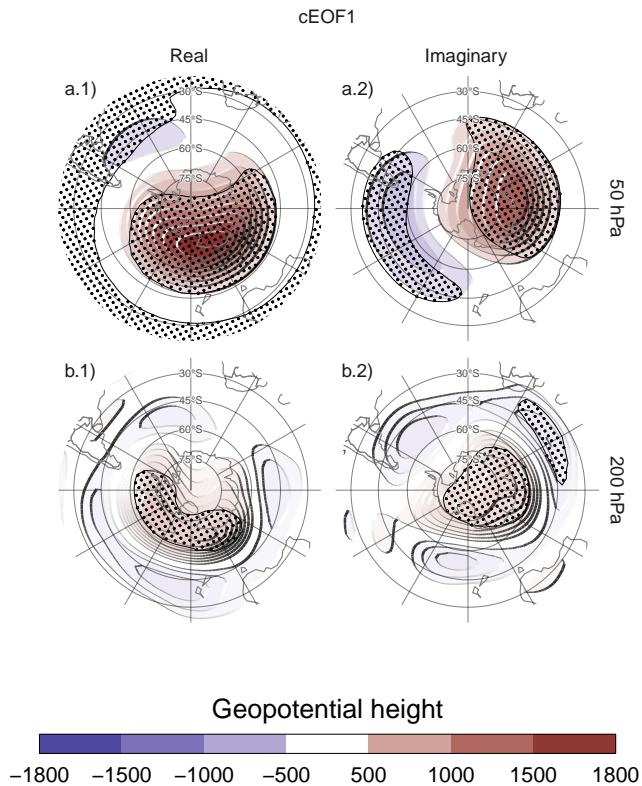


Fig. 3: Time series extended using ERA5 back extended preliminary edition (period 1950 – 1978) and ERA5 (period 1979 – 2019). Dark straight line is the OLS trend. Black horizontal and vertical line mark the mean value and range of each time series respectively.

`fig:extended-series`

que las que ya están, pero creo que sería una referencia útil para visualmente poder decir a qué año corresponde cada punto. Además, fíjate que la figura te quedó de un ancho mayor que el de la página y te quedó un "EOF" en el eje-y a la izquierda que no creo que sea lo más correcto.

There is only a significant upward trend in the real component of cEOF1 (Fig. 3a.1, p-value < 0.001) and no significant trend in any of the complex components of cEOF2. The positive trend in the real cEOF1 translates into a positive trend in cEOF1 magnitude, but not in the phase (not shown). This long-term change indicates an increase in the magnitude of the high latitude zonal wave 1. A similar observation was made by Raphael (2003), who detected a step after around 1975 in the leading EOF of August-September-October 500 hPa zonal geopotential height anomalies, which is similar to the cEOF1.



`fig:eof1-regr-gh`  
Fig. 4: Regression of SON geopotential height anomalies (meters) with the (column 1) real and (column 2) imaginary parts of the first cEOF for the 1979 – 2019 period at (row a) 50 hPa and (row b) 200 hPa. These coefficients come from multiple linear regression involving the real and imaginary parts. Areas marked with dots have p-values smaller than 0.05 adjusted for False Detection Rate.

### 302 3.2 cEOFs Regressions

303 The spatial patterns shown in Figure 2 are derived by removing the zonally  
 304 symmetric circulation, so they might not include all the variability that is actu-  
 305 ally associated with the cEOF time series. To understand the full geopotential  
 306 height field changes associated with each cEOF, we computed regression pat-  
 307 terns of the full geopotential fields onto each cEOF.

308 Figure 4 shows regression maps of SON geopotential height anomalies upon  
 309 cEOF1. At 50 hPa (Figure 4 row a), both the Real and Imaginary cEOF1 are  
 310 associated with planetary wave 1 patterns, that are 90° out of phase. Their  
 311 phases coincide with the ones shown in Figure 2a.1, with the positive centre  
 312 of the real cEOF1 located towards the dateline, and the one of the Imaginary  
 313 cEOF1 located over Eastern Antarctica. However, the Real cEOF1 pattern is

314 substantially altered by the zonally symmetric circulation. Instead of a clear  
 315 wave 1 pattern, the regression pattern can be better described as a monopole  
 316 with its centre displaced from the South Pole.

317 La figura 4 la veo muy saturada con los puntos que indican la significan-  
 318 cia. ¿se podrán hacer con un tamaño menor? ¿Las unidades son correctas?  
 319 Me llama la atención que te puedan dar tantos cientos de metros de altura  
 320 geopotencial.

321 The regression patterns for cEOF1 at 200 hPa (Figure 4 row b) are sim-  
 322 ilarly influenced by the zonally symmetric circulation. It is only possible to  
 323 partially distinguish the wave 1 pattern in relation with the real cEOF1 (Fig-  
 324 ure 4b.1). The imaginary cEOF1 shows a much more zonally symmetrical  
 325 pattern resembling the negative SAM phase.

326 With the exception of the imaginary cEOF1, it is clear that these patterns  
 327 are very different than the fully zonally asymmetric versions (Fig. 2), partic-  
 328 ularly at 200 hPa. Moreover, only in the stratosphere these patterns actually  
 329 show a distinguishable wave 1 pattern shifted in phase by 90°, suggesting that  
 330 using the cEOF method is artificially generating a wave structure at 200hPa.  
 331 Therefore, the magnitude and phase of the cEOF1 are associated with the  
 332 magnitude and phase of a zonal wave only in the stratosphere. While in the  
 333 troposphere, they are associated with slightly off-centre monopoles.

334 Figure 5 shows the regression pattern of geopotential height anomalies  
 335 upon the cEOF2. Unlike for cEOF1, in this case the regression patterns are  
 336 similar to the fully zonally asymmetric patterns from Figure 2. Although there  
 337 are some differences (particularly in 50 hPa), the wave trains identified before  
 338 are well characterised and patterns associated with the real cEOF2 are 90°  
 339 out of phase with those associated with the imaginary cEOF2. Zonal wave  
 340 3 dominates all fields, but only in the western hemisphere, over the Pacific  
 341 and Atlantic Oceans. cEOF2 then represents an equivalent barotropic wave  
 342 train that is very similar to the the Pacific South American Patterns (Mo and  
 343 Paegle, 2001). Comparing the location of the positive anomaly near 90°W in  
 344 column b of Figure 5 with Figures 1.a and b from Mo and Paegle (2001), the  
 345 real cEOF2 can roughly be identified with PSA2, while the imaginary cEOF2  
 346 resembles PSA1.

347 **Figura 5. Me resultó raro que vaya hasta 999 en vez de 1000**

### 348 3.3 cEOFs relationship with known modes of variability

other-variables

#### 349 3.3.1 SAM

sam

350 To explore the relationship between SAM and the modes described from the  
 351 cEOF, we compute the coefficient of determination between the cEOFs time-  
 352 series and the three SAM indices (SAM, A-SAM and S-SAM) at each ver-  
 353 tical level (Fig. 6). The SAM index is statistically significant correlated with  
 354 the Real cEOF1 in all levels, and with the Imaginary cEOF1 and Imaginary

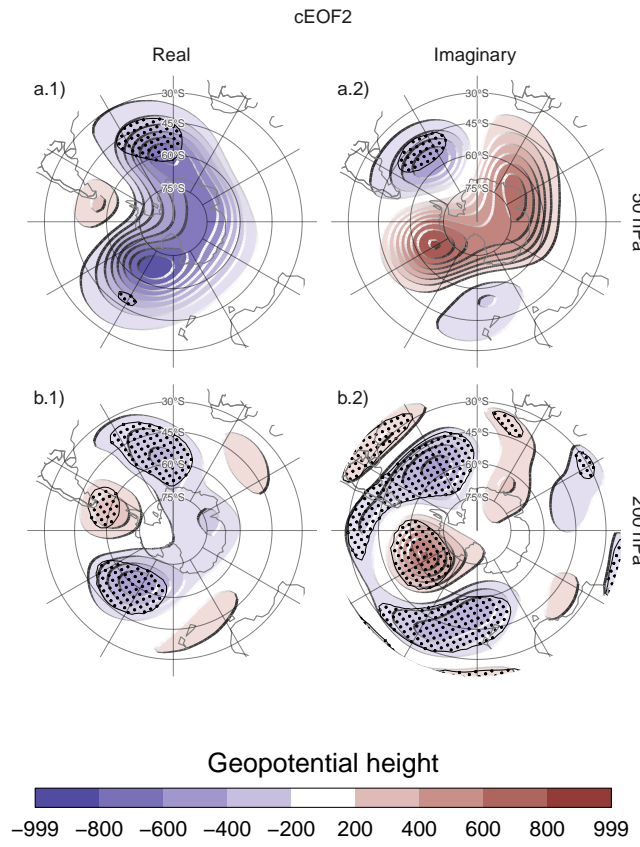


Fig. 5: Same as Figure 4 but for the second cEOF.

355 cEOF2 in the troposphere. Correlations between SAM and the Real cEOF2  
 356 are non-significant.

357 Fig. 6. Te quedan muy pegados los subplots de la columna izquierda con  
 358 los de la derecha. Recomendaría aumentar el espacio intermedio y repetir el  
 359 eje y en las figuras de la derecha. Además podrías agregar el y-label (Level) a  
 360 la izquierda.

361 The relationship between the tropospheric SAM and cEOF1 is explained  
 362 entirely by the zonally symmetric component of the SAM as shown by the low  
 363 and statistically non-significant correlations between the A-SAM and either  
 364 the Real or Imaginary cEOF1 and the high correlation with the S-SAM below  
 365 100 hPa. In the stratosphere, the Real cEOF1 is correlated with both A-  
 366 SAM and S-SAM, while the Imaginary cEOF1 is highly correlated only with  
 367 the A-SAM. These correlations are consistent with the regression patterns of  
 368 geopotential height in Figure 4 and their comparison with those obtained for  
 369 SAM, A-SAM and S-SAM by Campitelli et al (2021).

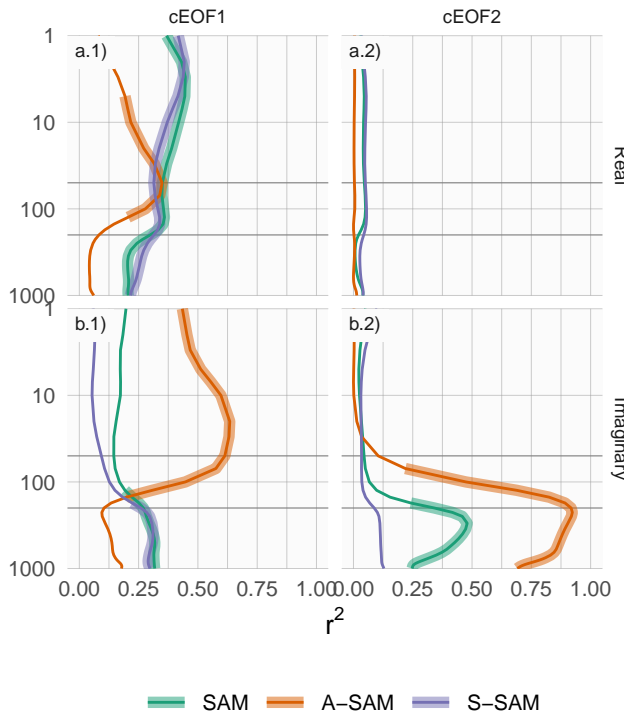


Fig. 6: <sup>fig:sam-eof-vertical</sup> Coefficient of determination between the real and imaginary part of each cEOF and the SAM, Asymmetric SAM (A-SAM) and Symmetric SAM (S-SAM) indices computed at each level according to Campitelli et al (2021). Thick lines represent estimates with  $p$ -value  $< 0.01$  corrected for False Detection Rate (Benjamini and Hochberg, 1995).

370 In the case of cEOF2, the moderate correlation between SAM and Imaginary  
 371 cEOF2 becomes extremely high only when the zonally asymmetric vari-  
 372 ability of the SAM is considered. The Imaginary cEOF2 explains up to 92% of  
 373 A-SAM variance, reached the maximum value at 225 hPa (Figure 6.b2). Such  
 374 extremely high correlation between the asymmetric SAM and the Imaginary  
 375 cEOF2 suggests that these might be different ways of characterising the same  
 376 phenomenon.

### 377 3.3.2 PSA

378 psa  
 Tabla 2. Mismo comentario que antes con lo del background color (no dice  
 379 mucho si no se conoce la escala), quizás puedes destacar en negritas según la  
 380 significancia. ¿Está bien el intervalo de confianza de PSA2 vs cEOF2 Im? Hay  
 381 algo raro ahí

382 Due to the similarity between the PSA patterns and the cEOF2 spatial  
 383 patterns (Fig. 5), we study the relationship between these modes. Table 2

Table 2: Correlations between the Real and Imaginary parts of cEOF2 and the PSA1 and PSA2 modes computed as the second and third EOFs of seasonal geopotential height anomalies (following Mo and Paegle, 2001) for the 1979 – 2019 period. 95% confidence intervals in parenthesis. Background colour indicates the value of correlation.

PC	cEOF2	
	Real	Imaginary
PSA1	-0.32 (CI: -0.57 – -0.015)	-0.82 (CI: -0.9 – -0.69)
PSA2	0.81 (CI: 0.67 – 0.9)	-0.062 (CI: -0.36 – 0.25)

384 shows the correlations between the two PSA indices and the timeseries for Real  
 385 and Imaginary phase of cEOF2. As anticipated by Figure 5, there is a strong  
 386 correlation between PSA1 and Imaginary cEOF2, and between PSA2 and Real  
 387 cEOF2. Conversely, there is no relationship between PSA1 and Real cEOF2,  
 388 and between PSA2 and Imaginary cEOF2. As a result, cEOF2 represents well  
 389 both the spatial structure and temporal evolution of the PSA modes, as well  
 390 as it is possible to make a rather clean association between its two phases  
 391 and the two PSA modes. So, It could be concluded that the same particular  
 392 rotation of cEOF2 that maximises the association between cEOF2 parts and  
 393 PSA modes, is the one which maximises the relationship between ENSO and  
 394 Imaginary cEOF2.

395 The reason the conventional EOF analysis arrives at the same separation  
 396 than our particular cEOF rotation is probably the fact that not all phases are  
 397 equally frequent. To visualize that, Figure 7 shows an histogram that counts  
 398 the number of SON years in which the cEOF2 was close to each of the four  
 399 particular phases (positive/negative Real/Imaginary), with the observations  
 400 for each season marked as rugs on the horizontal axis. For instance, years  
 401 with cEOF2 phase within  $45^\circ$  of  $0^\circ$  are nearest the “positive Real” phase.  
 402 About two thirds of time cEOF2 has a phase similar to either the negative  
 403 or positive Imaginary phase. It could be seen that Imaginary phase is the  
 404 most common phase and It is also, by construction, the direction that has the  
 405 maximum relationship with ENSO. Therefore, the Imaginary cEOF2 explains  
 406 more variance than the Real cEOF2 and conventional EOF analysis will tend  
 407 to separate the two.

408 The result obtained here is similar to the one obtained by Irving and Sim-  
 409 monds (2016). They show that the phase distribution of the PSA-like variabil-  
 410 ity obtained by them is bimodal and isolate the PSA pattern from the rest  
 411 of the PSA-like variability by selecting events that are near the peaks of the  
 412 distribution (compare our Figure 7 with their Figure 6).

413 The advantage of our method is that it is much simpler to implement,  
 414 it provides magnitude and phase naturally, and it facilitates the description  
 415 of this mode as a propagating wave instead of as standing oscillations. As a  
 416 consequence, the cEOF2 offers an alternative way of representing the PSA  
 417 which has several advantages over using the second and third EOFs.

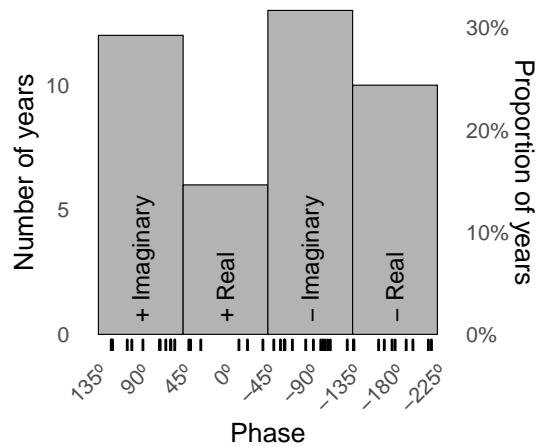


Fig. 7: `fig:phase-histogram` Histogram of phase distribution of cEOF2 for the 1979 – 2019 period. Bins are centred at  $90^\circ$ ,  $0^\circ$ ,  $-90^\circ$ ,  $-180^\circ$  with a binwidth of  $90^\circ$ . The small vertical lines near the horizontal axis mark the observations.

418    3.3.3 Temperature and Ozone

`temperature-and-ozone`

419    The relation between cEOFs and air temperature was also evaluated. Figure 420 shows regression patterns of air temperature at 50hPa and 200hPa onto 421 cEOF1. In both levels, the Real cEOF1 is associated with a positive monopole 422 over the South Pole with its centre moved slightly towards  $150^\circ\text{E}$  (Fig. 8 col- 423 umn 1). On the other hand, the regression maps on the Imaginary cEOF1 424 show a more clear wave 1 pattern with its maximum around  $60^\circ\text{E}$ . The distri- 425 bution of temperature regression coefficients at 50 hPa and at 200 hPa mirror 426 the geopotential height regression maps at 50 hPa (Fig. 4).

427    Figure 9 shows the vertical distribution of the regression coefficients on 428 cEOF1 from zonal anomalies of air temperature and zonal anomalies of ozone 429 mixing ratio averaged between  $75^\circ\text{S}$  and  $45^\circ\text{S}$ . Temperature zonal anomalies 430 associated with cEOF1 show a clear wave 1 pattern for both real and imaginary 431 components throughout the atmosphere above 250 hPa with a change in sign 432 above 10 hPa. Following hydrostatic balance, this is the level in which the 433 geopotential anomaly have maximum amplitude (not shown).

434    The maximum ozone anomalies are co-located with the minimum temper- 435 ature anomalies above 10 hPa and with the maximum temperature anomalies 436 below 10 hPa (Fig. 9). Therefore, the ozone zonal wave 1 is anticorrelated 437 with the temperature zonal wave 1 in the upper stratosphere, and directly 438 correlated in the upper stratosphere. This change in phase is observed in 439 ozone anomalies forced by planetary waves that reach the stratosphere. In 440 the photochemically-dominated upper stratosphere, cold temperatures inhibit 441 the destruction of ozone. On the other hand, in the advectively-dominated 442 lower stratosphere, ozone anomalies are  $90^\circ$  out of phase with horizontal and

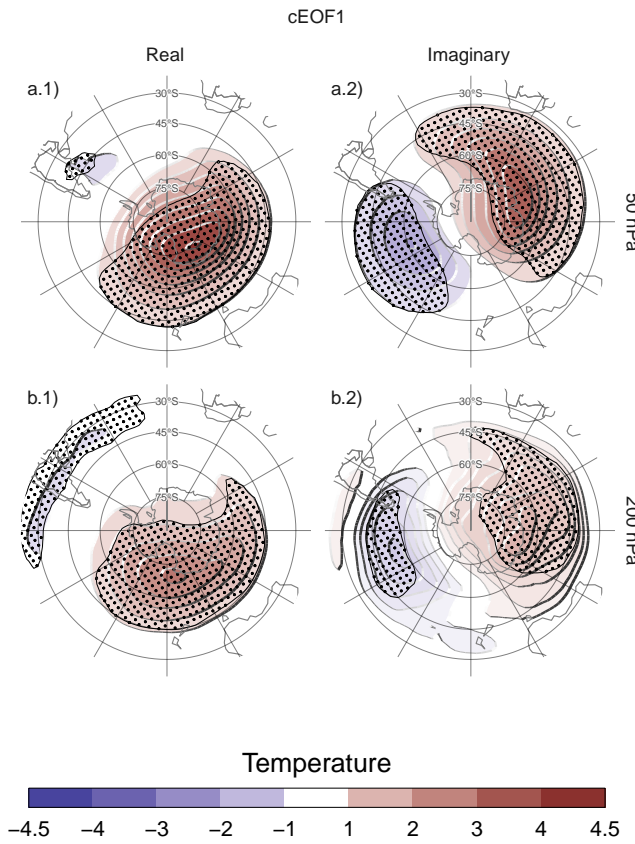


Fig. 8: Same as Figure 4 but for air temperature (K).

443 vertical transport, which are in addition  $90^\circ$  out of phase with temperature  
 444 anomalies (Hartmann and Garcia, 1979; Wirth, 1993; Smith, 1995).

445 **Revisa que tenes una inconsistencia en el uso de mayúsculas en Real/Imaginary**  
 446 porque a veces las usas y a veces no.

447 The regression maps of cEOF1 with fields of Total Ozone Column (TOC)  
 448 (Fig. 10) show zonal wave 1 patterns in TOC associated with both phases of  
 449 cEOF1. Climatologically, the springtime Ozone minimum is located off the  
 450 South Pole and towards the Weddell Sea (Grytsai, 2011). Thus, the Real  
 451 cEOF1 regression pattern (Figure 10a) coincides with the climatological po-  
 452 sition of the ozone hole while the one for the Imaginary cEOF1 is shifted by  
 453  $90^\circ$ .

454 There is a close spatial relationship between amplitudes and phases of the  
 455 cEOF1 and TOC planetary wave 1 between  $75^\circ\text{S}$  and  $45^\circ\text{S}$ . The correlation  
 456 between the amplitude of both indices is 0.77 (CI: 0.61 – 0.87) and 0.49 (CI:  
 457 0.21 – 0.69) between their phases.

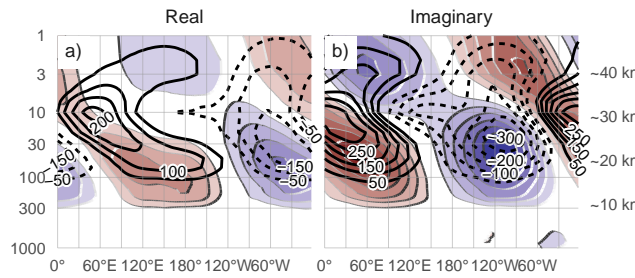


**Fig. 9:** Regression of SON anomalies of mean air temperature (shaded, Kelvin) and ozone mixing ratio (contours, negative contours with dashed lines, labels in parts per billion by mass) averaged between 75°S and 45°S with the (a) real and (b) imaginary parts of the first cEOF for the 1979 – 2019 period.

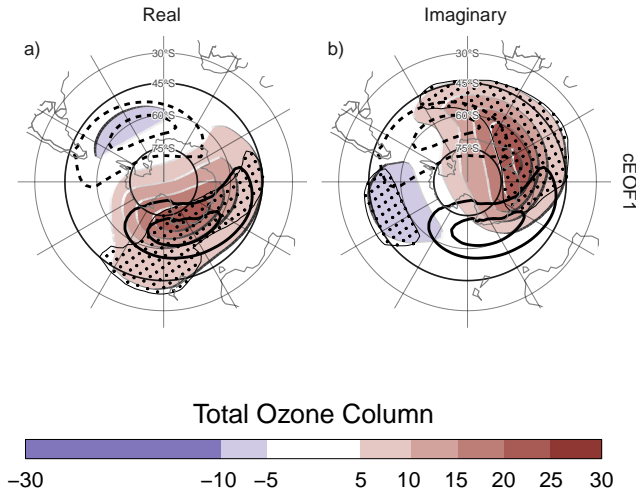


**Fig. 10:** Regression of SON mean Total Ozone Column anomalies (shaded, Dobson Units) with the (a) real and (b) imaginary parts of the cEOF1 for the 1979 – 2019 period. On contours, the mean zonal anomaly of Total Ozone Column (negative contours in dashed lines, Dobson Units). Areas marked with dots have p-values smaller than 0.05 adjusted for False Detection Rate.

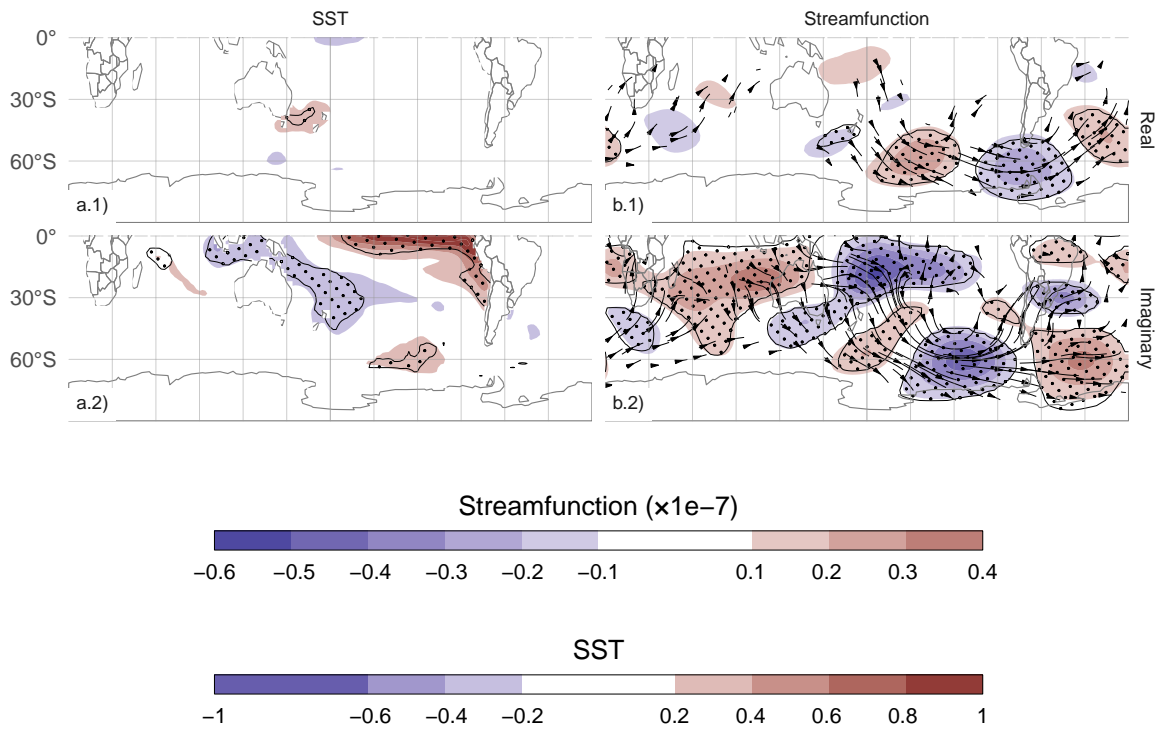


Fig. 11: Regression maps of cEOF2 with SST (column a) and streamfunction zonal anomalies (shaded) with their corresponding activity wave flux (vectors) (column b). Areas marked with dots have p-values smaller than 0.01 adjusted for FDR. *Agregar unidades. Quedaría mucho mejor el gráfico y creo que se prestaría a menos confusión si colocas las barras de colores en las columnas correspondientes. Otro detalle es que en gral. para el gráfico de streamfunction la escala de colores se usa al revés para que los azules (positivos) sean ciclónicos y los rojos anticiclónicos*

`fig:sst-psi-2`

#### 458 3.4 Tropical sources

459 The connections between cEOFs and Tropical sources are also assessed. Figure 11 shows the regression maps of Sea Surface Temperatures (SST) and  
 460 Streamfunction anomalies at 200 hPa respectively upon cEOF2. The Imaginary  
 461 cEOF2 is associated with strong positive SST anomalies on the Central  
 462 Pacific and negative anomalies over an area across the North of Australia and  
 463 New Zealand, the South Pacific Convergence Zone (SPCZ) (Figure 11.a2).  
 464 This pattern is almost canonically positive ENSO (Bamston et al, 1997) and  
 465 indeed, the correlation between the Imaginary cEOF2 and the Oceanic Niño  
 466 Index (Bamston et al, 1997) is significant and very high 0.76 (CI: 0.59 – 0.87).  
 467 Besides, the Imaginary cEOF2 is associated with strong wave-like streamfunc-  
 468 tion anomalies emanating from the tropics (Figure 11.b2). This is consistent  
 469

`tropical`

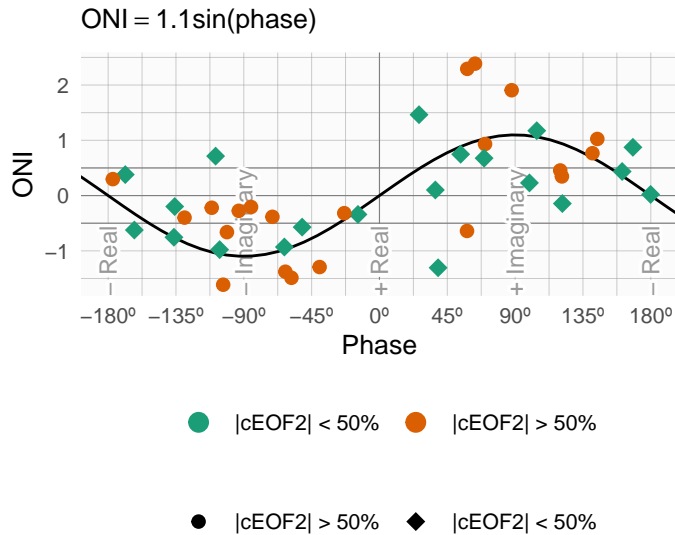


Fig. 12: `fig:enso-phase` ONI plotted against cEOF2 phase for the 1979 – 2019 period. Years with magnitude of cEOF2 greater or smaller than the 50th percentile are shown as orange circles and green diamonds respectively. Black line is the fit  $\text{ONI} \sim \sin(\text{phase})$  computed by weighted OLS using the magnitude of the cEOF2 as weights.

470 with the effect of ENSO on the extratropics: SST anomalies initiate anomalous  
 471 tropical convection that excites Rossby waves that propagate meridionally  
 472 towards higher latitudes (Mo, 2000).

473 Since the Real cEOF2 represents just a different phase of the same wave  
 474 train, it would be expected to show a similar forcing pattern to the Imaginary  
 475 cEOF2 with a slight translation of its location. However, Figure 11.a1 and b1  
 476 show that the Real cEOF2 is not associated either with any significant SST  
 477 nor streamfunction anomalies in the tropics. The correlation between the Real  
 478 cEOF2 and ENSO is also not significant (0.00025 (CI: -0.31 – 0.31)). **Usar**  
 479 **notación científica por la cantidad de 0 que tiene.** This lack of tropical signal  
 480 suggest that the Real cEOF2 and the Imaginary cEOF2 have very different  
 481 sources of variability.

482 To better explore the relationship between tropical forcing and phase of the  
 483 cEOF2, Figure 12 shows the ONI index against the cEOF2 phase for each SON  
 484 trimester between 1979 and 2019, highlighting years in which the magnitude  
 485 of cEOF2 is above the median. In years with positive ONI, the phase of the  
 486 cEOF2 is mostly around  $+90^\circ$  (corresponding with positive imaginary part)  
 487 and vice versa. In years with near neutral ENSO, the phase of the cEOF2  
 488 is much more variable. The black line in Figure 12 is a sinusoidal fit of the  
 489 relationship between ONI and cEOF2 phase. The  $r^2$  corresponding to the fit is  
 490 0.56, statistically significant with p-value  $< 0.001$ , indicating a quasi-sinusoidal  
 491 relation between these two variables.

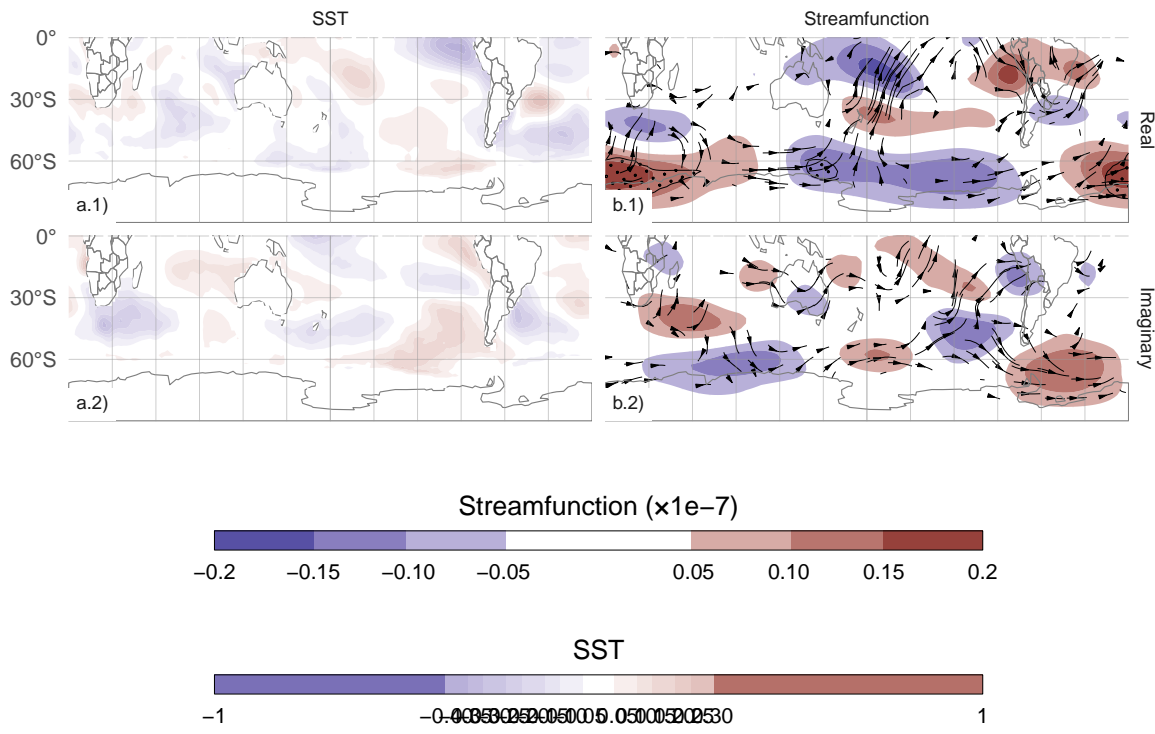


Fig. 13: Same as Figure 11 but for cEOF1. [fig:sst-psi-1](#)

492 Fig. 12 Revisa cómo te quedo abajo de la figura la indicación de qué son  
 493 cada uno de los puntos (te quedaron dos círculos y una línea extra que no va)

494 Furthermore, Figure 12 suggest that highest amplitude cEOF2 years tend  
 495 to coincide with strong ENSO years. The correlation between the absolute  
 496 magnitude of the ONI and the magnitude of the cEOF2 is 0.45 (CI: 0.17  
 497 – 0.67). This relationship, however, appears to be driven only by the three  
 498 years with strongest ENSO events in the period (2015, 1997, and 1982) which  
 499 also coincide with the three years with strongest cEOF2 magnitude. If those  
 500 years are removed, the correlation becomes non-significant (0.047 (CI: -0.28 –  
 501 0.36)). Furthermore, even when using all the datapoints, the Spearman corre-  
 502 lation –which is robust to outliers– is also non-significant (0.2, p-value= 0.21).  
 503 Therefore, the relationship between the magnitude of the cEOF2 train wave  
 504 and ONI remains uncertain.

505 It could be concluded that the wave train represented by cEOF2 can be  
 506 both part of the internal variability of the extratropical atmosphere or forced  
 507 by tropical SSTs. In the former case, the wave train has little phase preference.  
 508 However, when cEOF2 is excited by tropical SST variability, it tends to remain  
 509 locked to the imaginary phase. This explains the relative overabundance of  
 510 years with cEOF2 near positive and negative imaginary phase in Figure 7.

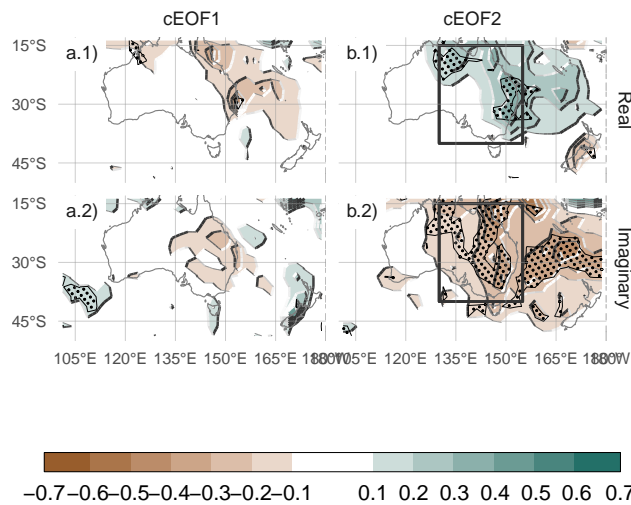


Fig. 14: <sup>fig:pp-oceania</sup> Regression of SON mean precipitation anomalies in Oceania (mm per day, shaded) and (column a) cEOF1 the (row 1) Imaginary and (column 1) Real phase. For the 1979 – 2019. Areas marked with dots have p-values smaller than 0.05 adjusted for False Detection Rate. In black is the West Australia region, defined as the box between 130°E and 155°E and 40°S and 15°S.

511     Figure 13 shows SST and streamfunction regression maps for cEOF1. Un-  
 512     like the cEOF2 case, there is no significant pattern of SST anomalies associ-  
 513     ated with either the Real or Imaginary cEOF1. Consistently, streamfunction  
 514     anomalies do not show any tropical influence. Instead, the real and imaginary  
 515     cEOF1 are associated with zonally wave activity fluxes in the extra-tropics  
 516     around 60°S, except for an equatorward flow from the coast of Antarctica  
 517     around 150°E in the real component. This suggests that it's variability is  
 518     driven primary by the internal variability of the extra-tropics.

519     Fig. 13 Tene en cuenta los mismos comentarios que en el figura 11 y revisa  
 520     también la barra de colores para SST que quedo rara

### 521     3.5 Precipitation

522     The influence of cEOFs variability in continental rainfall of extra-tropical  
 523     Southern Hemisphere is also explored. We focus on South America and Oceania  
 524     sectors because there are no relevant signals in southern Africa (not shown).

525     Revisa el caption de la figura 14 que quedo un estilo distinto que los  
 526     anteriores. Te falto aclarar también qué es la caja (¿la inventaste vos o habías  
 527     utilizado la de algún otro trabajo?). Fijate también de aumentar la separación  
 528     entre la columna izquierda y derecha para que no se superpongan los labels.  
 529     También fijate que esta barra de colores no te quedo con el borde externo como  
 530     el resto.

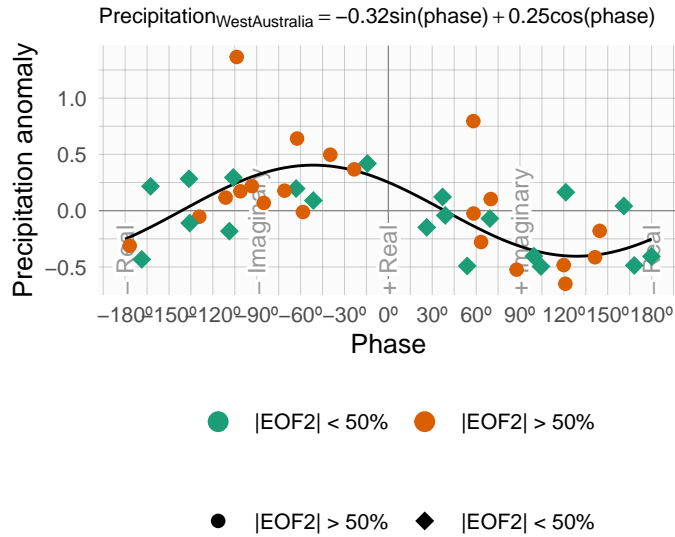


Fig. 15: Same as Figure 12 but for precipitation anomalies averaged between  $130^{\circ}\text{E}$  and  $155^{\circ}\text{E}$  and  $40^{\circ}\text{S}$  and  $15^{\circ}\text{S}$  (box shown in Figure 14 column b) in  $\frac{\text{mm}}{\text{day}}$ . Black line is the fit precipitation  $\sim \sin(\text{phase}) + \cos(\text{phase})$  computed by weighted OLS using the magnitude of the cEOF2 as weights.

531 The precipitation anomalies in Oceania associated with cEOF1 are weak  
 532 and not statistically significant (Figure 14 column a) whereas cEOF2 is associ-  
 533 ated with large and widespread anomalies. The Real cEOF2 is associated with  
 534 positive seasonal anomalies in Northern and Eastern Australia, and negative  
 535 ones over New Zealand, while precipitation anomalies associated with Imagin-  
 536 ary cEOF2 are negative over all Eastern Australia. As it could be expected,  
 537 these negative anomalies are similar to the springtime precipitation anomalies  
 538 observed in relation with the Asymmetric SAM (Campitelli et al, 2021) and  
 539 ENSO (Cai et al, 2011). **Acá te faltaría sacar un poco más el jugo asociando**  
 540 **con la figura 11. Además, ¿revisaste si podes también usar algún resultado**  
 541 **asociado a los PSA?**

542 **Revisa lo mismo que para la otra figura del tipo.**

543 To better understand the relationship between precipitation anomalies over  
 544 Eastern Australia and the cEOF2, Figure 15 plots precipitation anomalies av-  
 545 eraged over Eastern Australia (box in Figure 14) as a function of cEOF2 phase.  
 546 The black line shows a sinusoidal fit, whose coefficients are fitted by weighted  
 547 least squares using the magnitude of the EOF2 as weight. The  $r^2$  correspond-  
 548 ing to the fit is 0.41 (p-value  $< 0.001$ ). There is a strong relationship between  
 549 the phase of the cEOF2 and precipitation anomalies in Eastern Australia, but  
 550 the Real and Imaginary phases we chose are not exactly aligned with the direc-  
 551 tion that maximises this relationship. To perform a more in-depth analysis of  
 552 the relationship between this pattern and precipitation in this region, it would

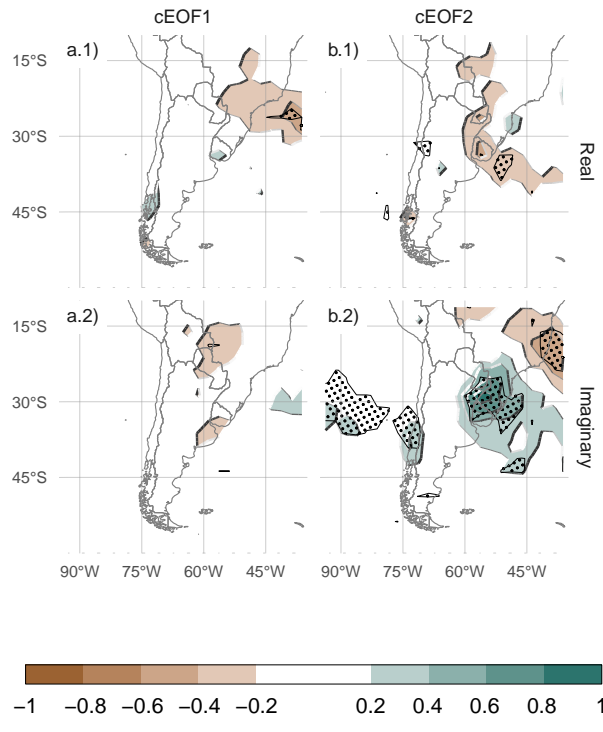


Fig. 16: As Figure 14 but for South America

553 be recommended to align one of the axis (either the Real or the Imaginary)  
 554 to the phase that maximises the described relationship.

555 Figure 16 shows regression maps of seasonal precipitation with each cEOF  
 556 in South America. cEOF1 is associated with negative regressions coefficients  
 557 for precipitation in Southern Brazil and Paraguay, although these are not  
 558 statistically significant (Fig. 16 column a). The strongest precipitation re-  
 559 gression coefficients are the ones associated with the Imaginary cEOF2. The  
 560 positive regression coefficients on Southeastern South America (SESA) and  
 561 Central Chile, and negative ones over South Atlantic Convergence Zone is  
 562 a well-known springtime precipitation signature of ENSO (Cai et al, 2020)  
 563 and it is also similar to the precipitation anomalies associated with the A-  
 564 SAM (Campitelli et al, 2021). **Lo mismo que te puse antes. Te faltaría sacar**  
 565 **un poco más el jugo asociando con la figura 11. Además, ¿revisaste si puedes**  
 566 **también usar algún resultado asociado a los PSA?**

567 This is not surprising considering the close relationship between the ONI,  
 568 the A-SAM index and the Imaginary cEOF2 shown previously, but further  
 569 consolidates the identification of this mode with the PSA pattern. On the other  
 570 hand, the Real cEOF2 is associated with negative precipitation anomalies  
 571 in a smaller area of SESA. Resembling the relationship between ONI and  
 572 the phase of cEOF2 (Fig. 12), there is a cEOF2 phase dependence of the

573 precipitation anomalies in SESA (not shown). These variables could be related  
574 wth a significant sinusoidal fit that has a statistically significant coefficient of  
575 determination of 0.27.

576 **4 Conclusions**

conclusions

577 In this study we assessed the Austral Spring Extratropical Southern Hemi-  
578 sphere zonally assymetric circulation. For this purpose, two complex indices  
579 were derived using Complex Empirical Orthogonal Functions. This allowed  
580 us to characterise both the amplitude and phase of planetary waves that are  
581 not perfectly organised as sinusoidal waves with constant amplitude at each  
582 latitude circle.

583 The first complex EOF represents the variability of the zonal wave 1 in  
584 the stratosphere, but represents a more zonally symmetric monopole in the  
585 troposphere. There is a statistically positive trend in the magnitude of this  
586 cEOF, which is consistent with previous studies that showed secular changes  
587 in springtime wave-1-like patterns (e.g. Raphael, 2003). This mode is closely  
588 related to stratospheric variability such as anomalies in Total Ozone Column.  
589 Otherwise, this complex EOF is not related with SST variability and conti-  
590 nental precipitation in the Southern Hemisphere.

591 The second complex EOF represents a wave-3 pattern with maximum mag-  
592 nitude in the Pacific sector. Essentially, it is an alternate representation of the  
593 PSA1 and PSA2 patterns (Mo and Paegle, 2001). We show that the Imagin-  
594 ary cEOF2 can be identified with the PSA1 and the Real cEOF2 with the  
595 PSA2. This cEOF prefers a phase aligned with the Imaginary cEOF2, because  
596 when ENSO is active, it forces the cEOF2 to be in the Imaginary phase. When  
597 ENSO is neutral, the cEOF2 is still active, but with no particular preferred  
598 phase. This mirrors the results of Cai and Watterson (2002), who showed that  
599 the CSIRO Model can create PSA-like variability even in the absence of ENSO  
600 forcing (with a climatological run), but the variability of one of the PSA modes  
601 was enhanced when adding the ENSO signal. The magnitude of the cEOF2  
602 appears not to be related to the magnitude of ENSO, except frot the three  
603 strongest ENSO events in the period which coincide with the three strongest  
604 cEOF2 years.

605 We further show that the Imaginary cEOF2 is closely related to the South-  
606 ern Annular Mode in the troposphere. In fact, it has a very close resemblance  
607 to the zonally asymmetric portion of the SAM. This raises the possibility that  
608 the asymmetric component of the SAM is actually a statistical contamination  
609 of the PSA mode.

610 Precipitation anomalies in South America associated with the Imaginary  
611 cEOF2 show a clear ENSO-like impact, with positive anomalies in South-  
612 Eastern South America, negative anomalies in Southern Brazil and positive  
613 anomalies in central Chile. Precipitation anomalies associated with the Real  
614 cEOF2 are low and not statistically significant, showing that the Imaginary

phase is optimally aligned with the direction of maximum precipitation impacts.

On the other hand, over Australia, both the Real and Imaginary phase are associated with significant precipitation anomalies, and we further show that the direction of maximum impact is not aligned with our chosen rotation of cEOF2. However, this underscores the benefit of using complex EOF, since it would be trivial to rotate it. *creo que esta idea convendría desarrollarla mejor para el que no lo tenga tan claro*

To the extent that the cEOF2 can be identified with the PSA, what is the advantage of the technique proposed here? The spatial fields that the cEOF2 index describes are in quadrature by construction, which makes it possible to derive a proper amplitude and phase. Furthermore, because of the way they are constructed, they are not forced to be orthogonal to the SAM. This makes it possible to study their relationship with the SAM free of the statistical contamination that comes with the usual definition of the PSA as the second and third EOFs.

Further work should extend this analysis to other seasons and further study the relationship between the cEOF2 and the SAM. In particular, it is not clear whether the close identification between the Imaginary cEOF2 and the Asymmetric SAM arises from physical processes or statistical contamination.

### Code availability

#### `code-availability`

A version-controlled repository of the code used to create this analysis, including the code used to download the data can be found at <https://github.com/eliocamp/shceof>.

## 5 References

#### `references`

### References

- Adams JC, Swartztrauber PN, Sweet R (1999) FISHPACK, a package of Fortran subprograms for the solution of separable elliptic partial differential equations. <https://www2.cisl.ucar.edu/resources/legacy/fishpack>
- Albers S, Campitelli E (2020) Rsoi: Import Various Northern and Southern Hemisphere Climate Indices
- Allaire JJ, Xie [aut Y, cre, McPherson J, Luraschi J, Ushey K, Atkins A, Wickham H, Cheng J, Chang W, Iannone R, Dunning A, filter] AYNsL, Schloerke B, Dervieux C, Aust F, Allen J, Seo J, Barrett M, Hyndman R, Lesur R, Storey R, Arslan R, Oller S, RStudio, PBC, library) jFj, library; authors listed in inst/rmd/h/jquery-AUTHORStxt) jcj, library; authors listed in inst/rmd/h/jqueryui-AUTHORStxt) jUcjU, library) MOB, library) JTB, library) BcB, Twitter, library) IB, library) AFh, js library) SJR, js library)

- 653 ISh, library) GFt, templates) JMP, Google, library) Ii, library) DRs, li-  
654 brary) Ws, Gandy (Font-Awesome) D, Sperry (Ionicons) B, (Ionicons) D,  
655 StickyTabs) ALj, filter) BPJpL, filter) AKpL (2020) Rmarkdown: Dynamic  
656 Documents for R
- 657 Baldwin MP, Thompson DWJ (2009) A critical comparison of stratosphere–  
658 troposphere coupling indices. *Quarterly Journal of the Royal Meteorological  
659 Society* 135(644):1661–1672, DOI 10.1002/qj.479
- 660 Bamston AG, Chelliah M, Goldenberg SB (1997) Documentation of a  
661 highly ENSO-related sst region in the equatorial pacific: Research note.  
662 *Atmosphere-Ocean* 35(3):367–383, DOI 10.1080/07055900.1997.9649597
- 663 Bell B, Hersbach H, Berrisford P, Dahlgren P, Horányi A, Muñoz Sabater  
664 J, Nicolas J, Radu R, Schepers D, Simmons A, Soci C, Thépaut  
665 JN (2020) ERA5 monthly averaged data on pressure levels from  
666 1950 to 1978 (preliminary version). Copernicus Climate Change Ser-  
667 vice (C3S) Climate Data Store (CDS) (Accessed on <19-02-2021>),  
668 [https://cds.climate.copernicus.eu/cdsapp#!/dataset/reanalysis-era5-  
669 pressure-levels-monthly-means-preliminary-back-extension?tab=overview](https://cds.climate.copernicus.eu/cdsapp#!/dataset/reanalysis-era5-pressure-levels-monthly-means-preliminary-back-extension?tab=overview)
- 670 Benjamini Y, Hochberg Y (1995) Controlling the False Discovery Rate: A  
671 Practical and Powerful Approach to Multiple Testing. *Journal of the Royal  
672 Statistical Society: Series B (Methodological)* 57(1):289–300, DOI 10.1111/j.  
673 2517-6161.1995.tb02031.x
- 674 Cai W, Watterson IG (2002) Modes of Interannual Variability of the South-  
675 ern Hemisphere Circulation Simulated by the CSIRO Climate Model. *Jour-  
676 nal of Climate* 15(10):1159–1174, DOI 10.1175/1520-0442(2002)015<1159:  
677 MOIVOT>2.0.CO;2
- 678 Cai W, van Rensch P, Cowan T, Hendon HH (2011) Teleconnection Pathways  
679 of ENSO and the IOD and the Mechanisms for Impacts on Australian Rain-  
680 fall. *Journal of Climate* 24(15):3910–3923, DOI 10.1175/2011JCLI4129.1
- 681 Cai W, McPhaden MJ, Grimm AM, Rodrigues RR, Taschetto AS, Garreaud  
682 RD, Dewitte B, Poveda G, Ham YG, Santoso A, Ng B, Anderson W, Wang  
683 G, Geng T, Jo HS, Marengo JA, Alves LM, Osman M, Li S, Wu L, Karam-  
684 peridou C, Takahashi K, Vera C (2020) Climate impacts of the El Niño–  
685 Southern Oscillation on South America. *Nature Reviews Earth & Environ-  
686 ment* 1(4):215–231, DOI 10.1038/s43017-020-0040-3
- 687 Campitelli E (2020) metR: Tools for Easier Analysis of Meteorological Fields
- 688 Campitelli E, Díaz LB, Vera C (2021) Assessment of zonally symmetric and  
689 asymmetric components of the Southern Annular Mode using a novel ap-  
690 proach. *Clim Dyn* DOI 10.1007/s00382-021-05896-5
- 691 Dowle M, Srinivasan A (2020) Data.table: Extension of 'data.frame'
- 692 Fogt RL, Marshall GJ (2020) The Southern Annular Mode: Variability, trends,  
693 and climate impacts across the Southern Hemisphere. *WIREs Climate  
694 Change* 11(4):e652, DOI 10.1002/wcc.652
- 695 Gong D, Wang S (1999) Definition of Antarctic Oscillation index. *Geophysical  
696 Research Letters* 26(4):459–462, DOI 10.1029/1999GL900003
- 697 Grytsai A (2011) Planetary wave peculiarities in Antarctic ozone distribution  
698 during 1979–2008. *International Journal of Remote Sensing* 32(11):3139–

- 699 3151, DOI 10.1080/01431161.2010.541518
- 700 Hartmann DL, Garcia RR (1979) A Mechanistic Model of Ozone Transport  
701 by Planetary Waves in the Stratosphere. *Journal of the Atmospheric Sci-  
702 ences* 36(2):350–364, DOI 10.1175/1520-0469(1979)036<0350:AMMOOT>  
703 2.0.CO;2
- 704 Hersbach H, Bell B, Berrisford P, Biavati G, Horányi A, Muñoz Sabater J,  
705 Nicolas J, Peubey C, Radu R, Rozum I, Schepers D, Simmons A, Soci C, Dee  
706 D, Thépaut JN (2019) ERA5 monthly averaged data on pressure levels from  
707 1979 to present. Copernicus Climate Change Service (C3S) Climate Data  
708 Store (CDS) (Accessed on <08-03-2021>), DOI 10.24381/cds.6860a573
- 709 Hobbs WR, Raphael MN (2010) Characterizing the zonally asymmetric com-  
710 ponent of the SH circulation. *Clim Dyn* 35(5):859–873, DOI 10.1007/s00382-  
711 009-0663-z
- 712 Horel JD (1984) Complex Principal Component Analysis: Theory and Exam-  
713 ples. *Journal of Applied Meteorology and Climatology* 23(12):1660–1673,  
714 DOI 10.1175/1520-0450(1984)023<1660:CPCATA>2.0.CO;2
- 715 Huang B, Thorne PW, Banzon VF, Boyer T, Chepurin G, Lawrimore JH,  
716 Menne MJ, Smith TM, Vose RS, Zhang HM (2017) Extended Reconstructed  
717 Sea Surface Temperature, Version 5 (ERSSTv5): Upgrades, Validations, and  
718 Intercomparisons. *Journal of Climate* 30(20):8179–8205, DOI 10.1175/JCLI-  
719 D-16-0836.1
- 720 Hufkens K (2020) Ecmwfr: Programmatic interface to the two European Cen-  
721 tre for Medium-Range Weather Forecasts API services
- 722 Irving D, Simmonds I (2015) A Novel Approach to Diagnosing Southern  
723 Hemisphere Planetary Wave Activity and Its Influence on Regional Climate  
724 Variability. *Journal of Climate* 28(23):9041–9057, DOI 10.1175/JCLI-D-15-  
725 0287.1
- 726 Irving D, Simmonds I (2016) A New Method for Identifying the Pacific–South  
727 American Pattern and Its Influence on Regional Climate Variability. *Journal*  
728 of *Climate* 29(17):6109–6125, DOI 10.1175/JCLI-D-15-0843.1
- 729 Katz RW, Brown BG (1991) The problem of multiplicity in research on  
730 teleconnections. *International Journal of Climatology* 11(5):505–513, DOI  
731 10.1002/joc.3370110504
- 732 Marshall GJ (2003) Trends in the Southern Annular Mode from Observations  
733 and Reanalyses. *J Climate* 16(24):4134–4143, DOI 10.1175/1520-0442(2003)  
734 016<4134:TITSAM>2.0.CO;2
- 735 Mo KC (2000) Relationships between Low-Frequency Variability in the South-  
736 ern Hemisphere and Sea Surface Temperature Anomalies. *Journal of Cli-  
737 mate* 13(20):3599–3610, DOI 10.1175/1520-0442(2000)013<3599:RBLFVI>  
738 2.0.CO;2
- 739 Mo KC, Paegle JN (2001) The Pacific–South American modes and their down-  
740 stream effects. *International Journal of Climatology* 21(10):1211–1229, DOI  
741 10.1002/joc.685
- 742 Plumb RA (1985) On the Three-Dimensional Propagation of Stationary  
743 Waves. *J Atmos Sci* 42(3):217–229, DOI 10.1175/1520-0469(1985)042<0217:  
744 OTTDPO>2.0.CO;2

- 745 R Core Team (2020) R: A Language and Environment for Statistical Comput-  
746 ing. R Foundation for Statistical Computing, Vienna, Austria
- 747 Raphael M (2003) Recent, Large-Scale Changes in the Extratropical Southern  
748 Hemisphere Atmospheric Circulation. *J Climate* 16(17):2915–2924, DOI  
749 10.1175/1520-0442(2003)016<2915:RLCITE>2.0.CO;2
- 750 Raphael MN (2004) A zonal wave 3 index for the Southern Hemisphere. *Geo-*  
751 *physical Research Letters* 31(23), DOI 10.1029/2004GL020365
- 752 Raphael MN (2007) The influence of atmospheric zonal wave three on  
753 Antarctic sea ice variability. *Journal of Geophysical Research: Atmospheres*  
754 112(D12), DOI 10.1029/2006JD007852
- 755 Smith AK (1995) Numerical simulation of global variations of temperature,  
756 ozone, and trace species in the stratosphere. *Journal of Geophysical Re-*  
757 *search: Atmospheres* 100(D1):1253–1269, DOI 10.1029/94JD02395
- 758 Trenberth KE (1980) Planetary Waves at 500 mb in the Southern Hemisphere.  
759 *Mon Wea Rev* 108(9):1378–1389, DOI 10.1175/1520-0493(1980)108<1378:  
760 PWAMIT>2.0.CO;2
- 761 Trenberth KF, Mo KC (1985) Blocking in the Southern Hemisphere. *Mon Wea*  
762 *Rev* 113(1):3–21, DOI 10.1175/1520-0493(1985)113<0003:BITSH>2.0.CO;  
763 2
- 764 Turner J, Hosking JS, Bracegirdle TJ, Phillips T, Marshall GJ (2017) Variabil-  
765 ity and trends in the Southern Hemisphere high latitude, quasi-stationary  
766 planetary waves. *International Journal of Climatology* 37(5):2325–2336,  
767 DOI 10.1002/joc.4848
- 768 van Loon H, Jenne RL (1972) The zonal harmonic standing waves in the  
769 southern hemisphere. *Journal of Geophysical Research* 77(6):992–1003, DOI  
770 10.1029/JC077i006p00992
- 771 Walker SGT (1914) Correlation in Seasonal Variations of Weather, III: On the  
772 Criterion for the Reality of Relationships Or Periodicities. Meteorological  
773 Office
- 774 Wickham H (2009) Ggplot2: Elegant Graphics for Data Analysis. Use R!,  
775 Springer-Verlag, New York, DOI 10.1007/978-0-387-98141-3
- 776 Wilks D (2011) Statistical Methods in the Atmospheric Sciences, vol 100.  
777 Elsevier, DOI 10.1016/B978-0-12-385022-5.00022-1
- 778 Wilks DS (2016) “The Stippling Shows Statistically Significant Grid Points”:  
779 How Research Results are Routinely Overstated and Overinterpreted, and  
780 What to Do about It. *Bull Amer Meteor Soc* 97(12):2263–2273, DOI 10.  
781 1175/BAMS-D-15-00267.1
- 782 Wirth V (1993) Quasi-stationary planetary waves in total ozone and their  
783 correlation with lower stratospheric temperature. *Journal of Geophysical*  
784 *Research: Atmospheres* 98(D5):8873–8882, DOI 10.1029/92JD02820
- 785 Xie P, Arkin PA (1997) Global Precipitation: A 17-Year Monthly Analysis  
786 Based on Gauge Observations, Satellite Estimates, and Numerical Model  
787 Outputs. *Bull Amer Meteor Soc* 78(11):2539–2558, DOI 10.1175/1520-  
788 0477(1997)078<2539:GPAYMA>2.0.CO;2
- 789 Xie Y (2015) Dynamic Documents with R and Knitr, 2nd edn. Chapman and  
790 Hall/CRC, Boca Raton, Florida